Research Square

Preprints are preliminary reports that have not undergone peer review.
They should not be considered conclusive, used to inform clinical practice,
or referenced by the media as validated information.

Catalytic Conversion of Lignin in an Isopropanol/formic Acid Medium With Nimo Catalyst Promoted by W Species

Xinyu Lu
Nanjing Forestry University
Hossain Mahmud Robin
Nanjing Forestry University
Haoquan Guo
Nanjing Forestry University
Dandan Wang
Nanjing Forestry University
Pengcheng Xiu
Nanjing Forestry University
Jiajia Chen
Nanjing Forestry University
Yu Qin
Nanjing Forestry University
Chaozhong Xu
Nanjing Forestry University
Xiaoli Gu (guxiaoli@njfu.edu.cn)
Nanjing Forestry University https://orcid.org/0000-0001-8588-0358

Research Article

Keywords: Lignin, Formic acid, NiMo catalyst, HDO, Alkyl guaiacols

Posted Date: May 27th, 2021

DOI: https://doi.org/10.21203/rs.3.rs-533979/v1

License: This work is licensed under a Creative Commons Attribution 4.0 International License.
Read Full License

Catalytic conversion of lignin in an isopropanol/formic acid medium with NiMo catalyst promoted by W species

Xinyu Lu, Hossain Mahmud Robin, Haoquan Guo, Dandan Wang, Pengcheng Xiu, Jiajia Chen, Yu Qin, Chaozhong Xu *, Xiaoli Gu *

Co-Innovation Center for Efficient Processing and Utilization of Forest Products, College of Chemical Engineering, Nanjing Forestry University, 159 Longpan Road, Nanjing, 210037, P. R. China

* E-mail: xucz@njfu.edu.cn; guxiaoli@njfu.edu.cn

Abstract

Background: Large amounts of enzymatic hydrolysis lignin (EHL) are generated with the production of cellulosic bioethanol. Efficient degradation and upgrading of EHL is significant for the sustainable and stable development of energy supply.

Results: In this study, hydrodeoxygenation (HDO) of EHL to biofuels was carried out promoted by the *in situ* hydrogen donor produced from the decomposition of formic acid over NiMo catalysts. Results showed that active sites (derived from the support SiO_2, W, and NiMo species) had remarkable effect on lignin conversion, and the highest oil yield (57.2 wt%) was gained over NiMo/W-SiO_2 catalyst.

Conclusions: The product evolution demonstrated that active metal sites (derived from NiMo species) favored hydrogenolysis and deoxygenation via leading *in situ* hydrogen to attack C-O-C bonds, while acid sites (derived from the support) adsorbed and activated chemical bonds in lignin, resulting in the linkage cleavage caused by the heating program. The obtained bio-oil was rich in alkyl guaiacols (6.7 wt%), containing stable chemical properties and high quality.

Keywords: Lignin; Formic acid; NiMo catalyst; HDO; Alkyl guaiacols

Background

Nowadays, fossil-derived resources are the primary source of energy and commercial chemicals in human life. Therefore, the exploration of their substitutes has become a hotspot, especially for the development of bioenergy derived from biomass materials due to their low cost and broad distribution [1-3]. Lignocellulosic biomass, an abundant type of biomass, has drawn considerable attention due to its potential for liquid biofuels and valuable chemicals production [4]. Lignocellulosic biomass consists of three main components, namely cellulose (30-35 %), hemicellulose (20-35 %), and lignin (15-20 %) [5]. Among them, cellulose and hemicellulose can be effectively converted to gasoline, jet fuels, and diesel range hydrocarbons [6]. Lignin, a naturally aromatic polymer composed of three phenylpropane units (e.g., coniferyl, para-coumaryl, and sinapyl alcohols) which are cross-linked via various bonds (including β-O-4, α-O-4, 4-O-5, β-β, β-1, and 5-5 bonds), can be a prospective resource of aromatic compounds (which are normally obtained from fossil-derived feed stocks). However, these aromatic compounds produced from lignin thermochemical treatment usually contain oxygen, which lowers their quality and limits their further application. Therefore, the elimination of oxygen in lignin-derived compounds is a challenge. At present, hydrodeoxygenation (HDO), using molecular hydrogen over a suitable catalyst, is an efficient hydrotreatment process to produce high-quality biofuels through effective lignin conversion and oxygen elimination.

During cellulosic bioethanol process, a large amount of residue rich in lignin, which is named as enzymatic hydrolysis lignin (EHL), is produced. Recently, the

pathway of EHL to biofuels is an attractive method to achieve its valuable application [7]. HDO is one of the most effective methods to degrade biomass to biofuels [8]. During HDO, most oxygen-containing components and unsaturated chemical bonds will be converted into saturated hydrocarbons. Therefore, biofuels rich in hydrocarbons can be obtained after HDO process, which have more stable chemical properties and higher energy density. However, the traditional HDO process will consume large amounts of hydrogen, which is expensive and unsafe. Therefore, the utilization of internal hydrogen donors, known as *in situ* HDO process, is introduced into lignin conversion process [9, 10]. For instance, Li et al. reported the *in situ* HDO of enzymolysis lignin over NiMo based catalysts using aluminum-water reactions as *in situ* hydrogen donor, results illustrated that the yield of aromatic hydrocarbons in biofuels increased after *in situ* HDO process over $NiMoS/Al_2O_3$ catalyst [11].

At present, most of *in situ* hydrogen donors are organic solvents, such as formic acid and alcohols. Furthermore, nickel-molybdenum (NiMo) based catalysts, a promising candidate for hydrotreatment process, have been widely investigated on the conversion of lignin and upgrading of lignin-derived oils. For example, Priharto et al. reported a HDO treatment of lignin-derived bio-oils over NiMo catalysts, and results showed that with assistance of high-pressure molecular hydrogen, the content of oxygen was reduced from 23 wt% in raw oil to 7.5-11.5 wt% in hydrotreated oil after HDO [12]. Moreover, numerous studies also focused on the HDO of lignin-derived model compounds, such as guaiacol, phenol, and acetophenone [4, 13-15]. Therefore, the investigation of *in situ* HDO of raw lignin and internal reaction mechanism is

meaningful and beneficial for the development of biofuels and bioenergy.

In this experiment, to explore the *in situ* HDO process of EHL with assistance of formic acid performed as internal hydrogen donor over NiMo catalysts, and to further study the effect of W species incorporation on lignin depolymerization, a functional SiO_2 was prepared to be used as the support of NiMo catalysts which were utilized in EHL depolymerization. Comprehensive characterization was conducted to evaluate the physical and chemical properties of synthesized supports and NiMo catalysts, and to figure out the internal reaction mechanism of lignin depolymerization.

Results

Catalyst characterization

Fig. 1 N_2 adsorption-desorption isotherms of SiO_2-NC (a, uncalcined), SiO_2-C (b, calcined), Ti-SiO_2 (c), W-SiO_2 (d), and NiMo/W-SiO_2 (e). Respective pore size distributions of different samples (f: SiO_2-NC, g: SiO_2-C, h: Ti-SiO_2, i: W-SiO_2, and j: NiMo/W-SiO_2).

N_2-adsorption-desorption isotherms and pore size distribution of synthesized samples are presented in **Fig. 1**, and physical properties are shown in **Table 1**. As shown in **Fig. 1**, samples all exhibit type IV adsorption isotherm with H3 loop after calcination, indicating their mesoporous structure. The isotherms of Ti-/W-SiO_2 and NiMo/W-SiO_2 are similar with that of SiO_2-C with pronounced adsorption between 0.1 and 0.4, which is due to pore filling caused by capillary condensation [16]. This exhibits the presence of hexagonal cylindrical channels of synthesized support SiO_2 [17]. Meanwhile, for all samples (expect for SiO_2-NC) hysteresis loop is recorded, which is related to capillary

condensation in mesopores. However, the adsorption in the same range (0.1-0.4) for SiO_2-NC is slow without obvious hysteresis loop, which is due to pore blocking cause by the presence of surfactant (CTMAB), therefore, causing the uneven distribution of pore size (**Fig. 1f**). Calcination at 550 ºC is an effective method to remove CTMAB, leading to an increasing N_2 adsorption, an enlarged surface area (**Table 1**), and a uniform distribution of pore size (~ 30 Å) (**Figs. 1g**). Furthermore, variations in pore volume and pore size displayed in **Table 1** also indicate the change in textural properties after calcination. With the incorporation of Ti/W species, the surface area decreases from 654.2 to ~ 400 m^2 g^{-1}, indicating the pore blocking, thus leading to a decrease in pore volume (from 0.5 to 0.3 cm^3 g^{-1}) and a decline in N_2 adsorption (**Figs. 1h, i**). Moreover, with the addition of NiMo species, a further decrease in pore volume and surface area can be observed, which indicates the formation of metal particles blocking internal pores. However, **Fig. 1e**) shows that N_2 adsorption of NiMo/W-SiO_2 increases significantly as compared to that of W-SiO_2, which is due to the formation of different porous structures derived from metal particles dispersed on the support surface [18].

The SEM images show that before calcination, the support particles are dispersed uniformly covered by a white shell-like material (CTMAB), leading to pore blocking and slow N_2 adsorption (**Fig. 2a**). After calcination, the real morphology with sintering is presented in **Fig. 2b**, and many small particles (SiO_2 particles) can be found on its rough surface. With the addition of Ti/W species (**Figs. 2c, d**), the rough surface with small particles can be also detected, and no obvious metal particles are observed, demonstrating the uniform dispersion of metal particles without agglomeration,

corresponding to the result of XRD. However, as NiMo species were incorporated in the system, many particles with larger size can be found obviously in **Fig. 2e** to make the surface rougher, indicating the formation of Ni/Mo metal nanoparticles.

Table 1 Physical properties and acid strength of synthesized catalysts.

Fig. 2 SEM images of SiO_2-NC (a), SiO_2-C (b), Ti-SiO_2 (c), W-SiO_2 (d), and NiMo/W-SiO_2 (e).

The coordination environment of the incorporated Ti and W species was detected by UV-visible spectroscopy and spectra are presented in **Fig. 3**. No intense adsorption is observed for SiO_2 absorption spectra, indicating no obvious ligand to metal charge transfer (LMCT) within hexagonal structure of SiO_2. However, in case of Ti-SiO_2, a strong absorption can be found at around 251 nm, revealing a charge transfer from 2p orbital in tetrahedrally linked oxygen to 3d orbital in Ti species, which is a characteristic peak of tetrahedral coordination environment of Ti^{4+} [19]. As for W-SiO_2, no obvious peaks of W^{4+} and W^{5+} are observed between 400-700 nm, in other words, W species of W-SiO_2 mainly exists in the form of 6-valent oxide (WO_3) [20, 21]. Therefore, an intense absorption at around 261 nm is due to LMCT between O^{2-} ligands and W^{6+} cations of WO_3 species linked to SiO_2 surface.

Fig. 3 UV-visible diffuse reflectance spectra (DRS) of supports.

Meanwhile, FTIR spectra of supports are presented in **Fig. 4**. Obviously, all samples show a broad peak at 1089 cm^{-1}, a sharp peak at 461 cm^{-1}, and a weak one at 806 cm^{-1}, which are assigned to the internal asymmetric stretching, bending vibration, and symmetric stretching of Si-O-Si linkage, respectively [22-24]. In addition, the peak

155 located at 1632 cm^{-1} is attributed to Si-OH group [25]. The curve of Ti/W-SiO_2 shows
156 the presence of Ti/W-O-Si at around 960 cm^{-1}, indicating that titanium/tungsten species
157 exists in tetrahedral structure via coordination, corresponding to the result of UV-DRS.
158 Additionally, incorporating metal oxides into SiO_2 support leads to the creation of
159 acidity (both *L* and *B* acid). The *B* acid was partially attributed to the coordination of
160 Si-OH group to *L* center. Therefore, the presence of Si-OH group is important for
161 obtaining abundant acidic sites.

162 **Fig. 4** FTIR spectra of synthesized supports.

163 For measuring the acidity of synthesized samples, NH_3-TPD was carried out. The
164 results shown in **Fig. 5** present that, SiO_2-C presents a sharp peak at 160 ºC and a weak
165 one at around 300 ºC, which are assigned to weak acid sites, mainly originating from
166 silicon center [26]. Grafting different metal oxides (TiO_2 and WO_3) on support surface
167 results in an increase in total amount of acidity (**Table 1**, increasing from 0.17 mmol g^{-1}
168 for SiO_2-C to ~ 0.4 mmol g^{-1} for Ti/W-SiO_2) [27]. W-SiO_2 exhibits a higher peak at
169 around 160 ºC as compared to SiO_2-C, indicating weak acidic sites derived from
170 hydroxyl group linked to silanol group which is associated with tungsten center via
171 oxygen bridge (W-O-Si) [28]. On the other hand, similar peaks can be also observed
172 for Ti-SiO_2, which is lower than those of W-SiO_2. It is suggested that with the
173 incorporation of metal cations into silica, acidity (including *L* and *B* acidity) in these
174 formed mixed oxides will be induced, which depends on the coordination of
175 incorporated heteroatom and its amount of addition (**Table 1**, 6.82 wt% for W, 2.28 wt%
176 for Ti) [29]. However, as Ti^{4+} species has the same state as Si^{4+}, thus leading to a weaker

177 effect for Ti-SiO_2. Therefore, more acidity in W-SiO_2 (0.485 mmol g^{-1}) has been
178 detected than that in Ti-SiO_2 (0.339 mmol g^{-1}). Catalyst support with higher acidity is
179 more beneficial for supported metal dispersion, lignin-derived oxygen-containing
180 groups adsorption, and C-O linkages breaking [30, 31], which make W-SiO_2 potential
181 for utilization as a support of NiMo catalysts during HDO process.

182 **Fig. 5** NH_3-TPD of SiO_2-C (blue line), Ti-SiO_2 (red line), and W-SiO_2 (black line).

183 SA-XRD patterns of supports are shown in **Fig. 6a**. Except for SiO_2-NC, all
184 samples exhibit a sharp diffraction peak at (100) reflection plane of SiO_2, indicating its
185 ordered hexagonal mesoporous structure [19]. Moreover, this characteristic diffraction
186 peak shifts from 2.1 º for SiO_2-NC to 2.8 º for SiO_2-C, indicating the structural change
187 occurring after calcination. With the incorporation of Ti/W, no obvious shift appears in
188 the diffraction peak at 2.8 º, confirming that the synthesized catalysts also show the
189 textural properties of SiO_2. Above observations are corresponding to the results
190 obtained from BET and SEM. Additionally, two broad diffraction peaks are observed
191 at 4 and 4.8 º for SiO_2-C, which are assigned as a long-range array of hexagonal
192 cylindrical porous structure [19]. However, these two peaks are absent after metal
193 incorporation, suggesting a deterioration of the hexagonal structure as a result of
194 isomorphic substitution [32].

195 WA-XRD patterns of support and NiMo supported catalysts are shown in **Fig. 6b**.
196 A broad peak at the range of 15-40 º (2θ) is assigned to amorphous silica, while no
197 significant crystalline phase of WO_x is detected by WA-XRD, indicating the uniform
198 dispersion of W species. On the other hand, for NiMo/SiO_2 diffraction peaks at 2θ =

199 23.4, 25.7, and 27.3 º are observed and correspond to (110), (040), and (021) planes of
200 MoO_3 (orthorhombic crystalline phase) [33]. As compared to NiMo/SiO_2, no obvious
201 peaks for Mo species and lower diffraction peaks at 37.3, 43.4, and 62.9 º originate
202 from the reflection planes of (111), (200), and (220) of cubic phase of NiO can be
203 observed in NiMo/W-SiO_2 [34]. Above results indicate that the introduction of W
204 species is beneficial for metal dispersion, especially for Mo species, which is
205 corresponding to the result obtained in NH_3-TPD.

206 For NiMo/W-SiO_2, in order to get more information on doped species (Ni and Mo),
207 especially for the non-detected one (Mo) by XRD analysis, Raman spectra have been
208 performed. As shown in **Fig. 6c**, a pronounced peak located at 952 cm^{-1} coupled with a
209 weak one at 706 cm^{-1} is detected which is due to the presence Ni species, while bands
210 appearing at 821 and 896 cm^{-1} indicate the generation of crystalline MoO_3 nanoparticles
211 and the exist of MoO_4^{2-}, respectively [35]. The presence of MoO_4^{2-} derived from the
212 depolymerization of $Mo_7O_{24}^{6-}$ illustrates the improved dispersion of Mo species in
213 NiMo/W-SiO_2, leading to no obvious diffraction peaks appearing in XRD pattern [36-
214 38].

215 The results of H_2-TPR of NiMo/W-SiO_2 are shown in **Fig. 6d**. As depicted in **Fig.**
216 **6d**, a sharp peak at around 300-500 ºC is recorded, which is the characteristic adsorption
217 of the reduction of Mo^{6+} to Mo^{4+} species, while one small peak at around 600-700 ºC
218 is assigned to the characteristic peak of NiO species reduction, which is bound to
219 support surface weakly [39, 40].

220 **Fig. 6** (a) SA-XRD patterns of support and catalysts, (b) WA-XRD patterns of support

and NiMo supported catalysts, (c) Raman spectrum of NiMo/W-SiO_2, and (d) H_2-TPR profile of NiMo/W-SiO_2.

Lignin depolymerization

In this section, the effects of NiMo species and W promoter on lignin depolymerization were evaluated via lignin conversion, yields of bio-oil, char, and residual lignin (wt%). As shown in **Fig. 7**, the highest yield of bio-oil (57.2 wt%) is obtained over NiMo/W-SiO_2 catalyst, while that over SiO_2 is only 18.2 wt%, indicating the worse performance of SiO_2 on lignin catalytic conversion. However, as compared to non-catalyst system, the introduction of SiO_2 also makes positive effect on lignin conversion and bio-oil production. For NiMo/SiO_2, with the incorporation of NiMo species, the hydrotreatment ability is improved, resulting in the increase of bio-oil yield (from 18.2 wt% for SiO_2 to 46.3 wt% for NiMo/SiO_2) and a decrease in lignin residue (from 75.4 wt% for SiO_2 to 45.8 wt% for NiMo/SiO_2). It is suggested that the presence of active metal sites is beneficial for leading H• (derived from the decomposition of formic acid and alcoholic solvent) to attack oxygen-containing groups and C-O linkages, thus resulting in effective lignin depolymerization. Furthermore, the higher acidity produced by W promoter (as discussed via NH_3-TPD) favors adsorption and activation of chemical bonds (including C-C and C-O bonds in lignin), resulting in the linkage cleavage caused by heating program [41-43]. Therefore, abundant acidity coupled with active metal sites make NiMo/W-SiO_2 more effective for lignin depolymerization. On the other hand, with the increase of acid strength, re-polymerization of lignin fragments to form char occurs easier, resulting in the slight increase of char yield ($\leq$ 10 wt%).

Fig. 7 Catalytic evaluation of lignin depolymerization over different synthesized catalysts.

Recyclability test of catalyst

For testing the recyclability of catalyst, lignin depolymerizaiton was performed at the same condition over NiMo/W-SiO_2 for five times and each experiment was conducted for three times, and catalytic evaluation is presented in **Table 2**. With the increase of catalyst recyclability, surface area decreases dramatically with a decrease in pore volume, that is due to the blocking of porous structure caused by the coke deposition. Therefore, previously textural properties reappear with 321.2 m^2 g^{-1} of surface area and 0.26 cm^3 g^{-1} of pore volume after calcination. Although the catalyst NiMo/W-SiO_2 contains excellent metal anchoring capacity, deteriorated performance on lignin conversion indicates a worse catalytic ability of catalyst, which is due to the coverage of active metal and acidic sites after reaction. After calcination for catalyst reactivation, previously porous structure and catalytic sites all reappear, leading to an extra rise of bio-oil yield and lignin conversion. However, the catalytic performance of reactivation catalyst is worse than that of fresh one due to active phases sintering and leaching.

Table 2. Physical properties of spent catalyst and reactivated one.

Discussion

Reaction mechanism

Fig. 8 presents the main phenolic monomers obtained from lignin depolymerization. A large proportion of oxygen-containing guaiacols (G5-7) are identified over SiO_2 (6.7 wt%), leading to a low yield (1.0 wt%) of alkyl guaiacols (G1-4), indicating that less

hydrodeoxygenation pathway appears. With the addition of active metals (NiMo species), the hydrodeoxygenation ability of catalyst is improved, reflected in the increase of alkyl guaiacols yield (8.9 wt%). There are two main reasons for its improvement: (I) Mo^{4+} species in reduced Mo oxides formed at low reduction temperature performs as electron deficient active sites, absorbing oxygen-containing guaiacol molecule on catalyst surface via coordinating with oxygen atom of C-O bonds, thus resulting in the activation of C-O bonds [44, 45]. (II) Ni species promotes the activation of molecular H_2 produced from the decomposition of formic acid and solvent [4]. Therefore, the cooperation between Ni and Mo^{4+} species enhances HDO performance of lignin depolymerization, thus leading to an increasing trend of alkyl guaiacols. Furthermore, the higher acidity provided by W promoter can further enhance the adsorption and activation of chemical bonds, leading to the further conversion of 2-methoxy-4-methylphenol to guaiacol via demethylation.

The depolymerization of lignin over NiMo/W-SiO_2 occurs through four main steps (**Fig. 9**): (I) direct depolymerization of lignin over SiO_2 with assistance of formic acid acting as internal hydrogen donor, (II) hydrodeoxygenation of oxygen-containing guaiacols over NiMo active species (the promotion of H_2 activation from Ni species and the adsorption of C-O bonds from reduced Mo oxides), (III) adsorption, activation, and cleavage of C-O bonds over acidic sites (from support and W species), and (IV) further demethylation of 2-methoxy-4-methylphenol via the cooperation of NiMo species and acidic sites.

Fig. 8 The main monomers (wt%) produced from lignin depolymerization over

NiMo/W-SiO_2 (G1: guaiacol, G2: 2-methoxy-4-methylphenol, G3: 4-ethylguaiacol, G4: 2-methoxy-4-(1-propyl)phenol, S1: 2,6-dimethoxyphenol, G5: vanillin, G6: 4-hydroxy-3-methoxyacetophenone, G7: 4-hydroxy-3-methoxypropiophenone).

Fig. 9 Possible reaction mechanism of lignin depolymerization over supported metal catalysts with assistance of formic acid used as an internal hydrogen donor.

Conclusions

The *in situ* HDO process of EHL with internal hydrogen source provided from the decomposition of formic acid was investigated over NiMo/W-SiO_2 catalyst. Due to the heating effect, the in situ hydrogen provided from formic acid was driven by active metal sites to participate in lignin conversion, where Ni favored the introduction of hydrogen in hydrotreatment, and Mo species preferred adsorbing C-O-C bonds on catalyst surface. In the absence of active metal sites, the degradation of lignin was mainly derived from the functionality of acidic sites which favored the absorption and activation of chemical bonds in lignin, leading to an initial decomposition of lignin.

Method

Materials

Lignin used was enzymatic hydrolysis lignin (EHL, with Mw and Mn of 3259 and 1385 g mol^{-1}, respectively), which was friendly provided from Shandong Longli Biotechnology Co., Ltd. (Shandong, China). Before experiments, EHL was purified via an alkali pretreatment to obtain the extracted lignin, because the presence of cellulose and hemicellulose would cause a negative effect on lignin depolymerization and the processing steps were presented in our previous research [46]. After that, the extracted

309 lignin was dried at 105 ºC for 12 h, and lignin used in the following experiment was
310 assigned to extracted lignin. The proximate, ultimate, and component analyses of raw
311 and extracted lignin are presented in **Table 3**.

312 **Table 3.** Proximate, ultimate, and component analyses of raw and extracted lignin.

313 **Synthesis of support**

314 Support SiO_2 was prepared according to a previous research with a molar ratio of
315 2:1:0.2:0.25 of NaOH (95 %):SiO_2 (99..99 %):TMAOH (tetramethylammonium
316 hydroxide, 25 % aqueous solution):CTMAB (cetyltrimethylammonium bromide, 99 %),
317 respectively [48]. Typically, NaOH/SiO_2 solution (solution I) was obtained by the
318 preparation of NaOH solution in 80 mL deionized water followed by the addition of
319 SiO_2. The mixed solution was stirred at 70 ºC (± 2 ºC) for 30 min to gain a transparent
320 phase. Afterwards, continuous stir was maintained until the solution was cooled down
321 to room temperature. Meanwhile, a surfactant solution (solution II) was produced with
322 determined amount of TMAOH in 150 mL deionized water followed by the addition of
323 CTMAB. After 30 min stir, solution I was dropwise added to solution II, and pH was
324 adjusted to 8-10 using diluted H_2SO_4 (0.25 mol L^{-1}), and then the obtained suspension
325 was kept at 70 ºC (± 2 ºC) for 2 h with magnetic agitation. Finally, the mixture was
326 aged at room temperature for 24 h, and the gel generated later was separated by filtration
327 and centrifuged for several times with deionized water until neutral, which was named
328 as SiO_2-NC (uncalcined). After being calcined at 550 ºC for 8 h with a heating rate of
329 1 ºC min^{-1}, the prepared sample was assigned to SiO_2-C (calcined). Except for TMAOH
330 (Aladdin, Shanghai, China), other chemical regents were all purchased from Macklin

(Shanghai, China).

Preparation of Ti/W incorporated SiO_2

The modification of synthesized support was carried out by wetness impregnation method [49], using titanium(IV) isopropoxide ($Ti(OiPr)_4$, 99.9 %) and ammonium metatungstate hydrate ($(NH_4)_6H_2W_{12}O_{40}.xH_2O$, 99.5 %) as metal precursors. In a typical process, SiO_2-C (5 g) was dispersed in 40 mL anhydrous ethanol (≥ 99.5 %), which initially dissolved determined amount of metal precursors to obtain nominal metal loading of 0.5 mmol Ti/W per SiO_2. The obtained suspension was maintained at room temperature with magnetic stir for 8 h. After that, the sample was filtered and washed with anhydrous ethanol for three times and dried at 75 °C overnight. Calcination process was performed at 500 °C for 4 h with a heating rate of 1 °C min^{-1}, and the obtained sample was named as Ti-/W-SiO_2. All chemicals used were all purchased from Macklin (Shanghai, China).

Preparation of NiMo supported catalyst

NiMo supported catalysts on SiO_2 and W/SiO_2, respectively, were prepared with total metal loading of 10 mmol Ni + Mo (Ni/Mo = 1:1, molar ratio) per support via co-impregnation method. In a typical synthesis, nickel(II) nitrate hexahydrate (99.9 %) and ammonium molybdate tetrahydrate (99.9 %) were employed as Ni and Mo precursors, respectively. After impregnation, the catalyst was dried as 105 °C for 6 h and calcined at 500 °C for 4 h with a heating rate of 1 °C min^{-1}. Before their utilization, NiMo supported catalysts were all reduced at 400 °C under H_2 (5 % H_2 in N_2). All chemicals used were purchased from Macklin (Shanghai, China).

Support and catalyst characterization

The physical properties (i.e., Brunauer-Emmett Teller (BET) surface area, pore volume, and pore size) and adsorption-desorption isotherms of synthesized samples were measured by a Tristar II series, micrometric analyzer at N_2 atmosphere (77K, -196 ºC). Surface area was determined using BET method and the distribution of pore size was calculated by BJH (Barret-Joyner-Halenda) method. The surface morphology of samples was recorded by scanning electron microscopy (SEM). UV-visible spectra of supports were performed in the range of 200-800 nm on a UV-2401PC Shimadzu spectrophotometer coupled with an integrating diffuse reflectance sphere (ISR 240A) and using $BaSO_4$ as reference material. The FTIR (Fourier Transform Infrared) was conducted on FTIR spectrometer (VERTEX 70 series, Bruker) with sample powder dispersed in KBr. NH_3-TPD (temperature programmed desorption) and H_2-TPR (temperature programmed reduction) were all performed on a Micromeritics AutoChem II 2920 automatic analyzer coupled with a thermal conductivity detector. Before NH_3 adsorption, the sample was treated *in situ* at 500 ºC for 30 min under He stream to eliminate water and other contaminants. Afterwards, the sample was cooled down to 120 ºC and contacted with He/NH_3 mixed gas (90/10, molar ratio) for 30 min with the flow rate of 20 mL min^{-1}. NH_3 desorption process was conducted in He stream with the flow rate of 20 mL min^{-1} at a heating rate of 10 ºC min^{-1} until reaching the temperature of 500 ºC. Before H_2 reduction experiment, the sample was pretreated *in situ* at 500 ºC for 2 h under air flow and cooled down to room temperature at Ar flow. The reduction process was conducted under Ar/H_2 mixture (90/10, molar ratio) with flow rate of 20

375 mL min^{-1} at a heating rate of 10 ºC min^{-1} from room temperature to 800 ºC. X-ray
376 diffractions (XRD) of synthesized supports were conducted via small angle (SA) X-ray
377 scattering diffractometer with Cu Kα (λ=0.1542 nm) (Bruker) in the degree range of
378 0.6-8 º with a step rate of 0.02 º s^{-1}. The wide angle (WA) XRD patterns of catalysts
379 were obtained on an X-ray diffractometer (Bruker D8 advance) equipped with Cu Kα
380 (λ=0.1542 nm) radiation run at 40 kV and 40 mA between 2 and 80 º with the same step
381 rate of SA-XRD. Raman spectra of samples were recorded on a Renishaw in Via Raman
382 Microscope spectrometer coupled with a laser source at 514 nm, at 200 mW power.

383 **Lignin depolymerization**

384 Lignin depolymerization experiment was performed in a stainless steel reactor with
385 magnetic stir (100 mL). In a typical experiment, lignin (0.5 g) and catalyst (0.5 g) were
386 added into isopropanol (50 mL, ≥ 99.9 %) with magnetic stir and dispersed by further
387 ultrasonic treatment for 10 min. After that, 5 mL formic acid was mixed with the
388 previous suspension with stir, and then the reactor was purged with He several times
389 (but not being pressurized) to check for leaks and remove internal air, and heated from
390 room temperature to 240 ºC with a heating rate of 10 ºC min^{-1} for 8 h. At the end of
391 reaction, the reactor was quenched with ice water and cooled down to room temperature.
392 Each experiment was repeated for three times ensure the reproducibility.

393 The obtained products were in components of gas, liquid, and solid (including
394 residual lignin, char, and catalyst). As the content of gaseous products was less than 1
395 wt% (based on initial weight of lignin), thus they were ignored in the following analysis.
396 In a typical separation step (**Fig. 10**), gaseous products were released into the air after

opening the reactor. Liquid and solid phases were separated by washing the reactor with 30 mL dichloromethane (DCM, 99.5 %) for three times followed by filtration. Subsequently, lignin derived bio-oil was formed by evaporation at 55 ºC and 160 mbar using a rotary evaporator to remove DCM, isopropanol, and water (generated during lignin depolymerization). Residual lignin was gained by washing solid phase with NaOH solution (20 mL, 0.25 mol L^{-1}) for three times, and collected via acid precipitation with a HCl solution (0.10 mol L^{-1}) followed by filtration. After being washed with deionized water and centrifuged for three times, the obtained unreacted lignin was dried at 105 ºC for 12 h. The spent catalyst (including catalyst and char) was obtained after separating residual lignin from solid phase, and used for catalyst recyclability test. Finally, the reactivation of spent catalyst was carried out by calcination at 500 ºC with a heating rate of 1 ºC min^{-1} for 2 h followed by H_2 flow reduction.

Fig. 10 Separation steps of depolymerized phases.

Depolymerized products analysis and measurement

The product analysis was performed by the application of gas chromatography-mass spectrometer (GC-MS, Agilent 7890 GC with an Agilent 5975 inert MS indicator, Agilent Technologies Inc., USA), coupled with a HP-INNOWAX capillary column (30 m × 0.25 mm × 0.25 μm). The injection of sample was 1 μL, and the identification of depolymerized products was based on NIST library. In a typical temperature program, internal oven temperature was started from 60 ºC, maintained for 2 min, to 250 ºC with a heating rate of 10 ºC min^{-1}, and kept for 10 min. The quantitative measurement of

mainly recorded products was measured by external standard method using analytical standard chemicals (e.g., guaiacol, 2-methoxy-4-methylphenol, 4-ethylguaiacol, 2-Methoxy-4-(1-propyl)phenol, 2,6-Dimethoxyphenol, vanillin, 4-hydroxy-3-methoxyacetophenone, 4-hydroxy-3-methoxypropiophenone). All chemicals used as standards were purchased from Aladdin (Shanghai, China), and high-purity gas (He, 99.999 %) used in the experiment was purchased from Nanjing Special Gas Factory Co., Ltd. (Nanjing, China).

Lignin conversion, yields of bio-oil, unreacted lignin, and char were determined by Eqs. (1)-(4), respectively. Furthermore, yields of main phenolic monomers (guaiacol, 2-methoxy-4-methylphenol, 4-ethylguaiacol, 2-Methoxy-4-(1-propyl)phenol, 2,6-Dimethoxyphenol, vanillin, 4-hydroxy-3-methoxyacetophenone, 4-hydroxy-3-methoxypropiophenone) were obtained by Eq. (5).

$$Lignin\ \ conversion(wt\%)=\left(\frac{weight\ \ of\ \ initial\ \ lignin-weight\ \ of\ \ residual\ \ lignin}{weight\ \ of\ \ initial\ \ lignin}\right)\times 100\% \quad (1)$$

$$Bio-oil(wt\%)=\left(\frac{weight\ \ of\ \ bio-oil}{weight\ \ of\ \ initial\ \ lignin}\right)\times 100\% \quad (2)$$

$$Unreacted\ \ lignin(wt\%)=\left(\frac{weight\ \ of\ \ residual\ \ lignin}{weight\ \ of\ \ initial\ \ lignin}\right)\times 100\% \quad (3)$$

$$Char(wt\%)=\left(\frac{weight\ \ of\ \ solid\ \ residue-weight\ \ of\ \ catalyst}{weight\ \ of\ \ initial\ \ lignin}\right)\times 100\% \quad (4)$$

$$Phenolic\ \ monomer(wt\%)=\left(\frac{weight\ \ of\ \ a\ \ phenolic\ \ monomer}{weight\ \ of\ \ initial\ \ lignin}\right)\times 100\% \quad (5)$$

Elemental analysis of lignin was conducted on CNH mode with a Vario EL III to determine the content of carbon, nitrogen and hydrogen, and that of oxygen was measured by difference.

List of abbreviations

EHL: enzymatic hydrolysis lignin; HDO: hydrodeoxygenation; SiO_2-NC (uncalcined);

SiO_2-C (calcined); LMCT: ligand to metal charge transfer; DRS: Diffuse Reflectance Spectra; TMAOH: tetramethylammonium hydroxide; CTMAB: cetyltrimethylammonium bromide; BET: Brunauer-Emmett Teller; BJH: Barret-Joyner-Halenda; SEM: Scanning Electron Microscopy; FTIR: Fourier Transform Infrared; NH_3-TPD: NH_3 Temperature Programmed Desorption; H_2-TPR: H_2 Temperature Programmed Reduction; XRD: X-Ray Diffractions; SA: Small Angle; WA: Wide Angle; DCM: dichloromethane; GC-MS: Gas Chromatography-Mass Spectrometer.

Declarations

Ethics approval and consent to participate

Not applicable

Consent for publication

Not applicable

Availability of data and materials

All data obtained in this study are included in this paper. Raw data are available on reasonable request.

Competing interests

The authors declare that they have no competing interests.

Funding

National Natural Science Foundation of China (no.21774059) and the Priority Academic Program Development (PAPD) of Jiangsu Higher Education Institutions.

Authors' contributions

Conceptualization, X.L.; methodology, H.M.R.; software, H.G.; validation, D.W., P.X. and J.C.; formal analysis, C.X.; investigation, X.G.; resources, X.G.; data curation, X.L.; writing-original draft preparation, X.L.; writing-review and editing, X.G.; visualization, H.M.R.; supervision, X.G.; project administration, C.X.; funding acquisition, X.G. All authors have read and agreed to the published version of the manuscript.

Acknowledgements

This research was financially supported by the National Natural Science Foundation of China (no.21774059), the Priority Academic Program Development (PAPD) of Jiangsu Higher Education Institutions, the opening funding of Jiangsu Key Lab of Biomass based Green Fuels and Chemicals.

References

1. Azadi P, Inderwildi OR, Farnood R, King DA. Liquid fuels, hydrogen and chemicals from lignin: A critical review. Renew Sustain Energ Rev. 2013;21:506-23. https://doi.org/10.1016/j.rser.2012.12.022.
2. Huber GW, Iborra S, Corma A. Synthesis of Transportation Fuels from Biomass: Chemistry, Catalysts, and Engineering. Chem Rev. 2006;106:4044-98. https://doi.org/10.1021/cr068360d.
3. Mortensen PM, Grunwaldt JD, Jensen PA, Knudsen KG, Jensen AD. A review of catalytic upgrading of bio-oil to engine fuels. Appl Catal A-Gen. 2011;407:1-19. https://doi.org/10.1016/j.apcata.2011.08.046.
4. Raikwar D, Munagala M, Majumdar S, Shee D. Hydrodeoxygenation of guaiacol over Mo, W and Ta modified supported nickel catalysts. Catal Today.

2019;325:117-30. https://doi.org/10.1016/j.cattod.2018.09.039.

5. Mood SH, Golfeshan AH, Tabatabaei M, Jouzani GS, Najafi G, Gholami M et al. Lignocellulosic biomass to bioethanol, a comprehensive review with a focus on pretreatment. Renew Sustain Energ Rev. 2013;27:77-93. https://doi.org/10.1016/j.rser.2013.06.033.
6. Alonso DM, Wettstein SG, Mellmer MA, Gurbuz EI, Dumesic JA. Integrated conversion of hemicellulose and cellulose from lignocellulosic biomass. Energ Environ Sci. 2013;6:76-80. https://doi.org/10.1039/c2ee23617f.
7. Tomás-Pejó E, Fermoso J, Herrador E, Hernando H, Jiménez-Sánchez S, Ballesteros M et al. Valorization of steam-exploded wheat straw through a biorefinery approach: Bioethanol and bio-oil co-production. Fuel. 2017;199:403-12. https://doi.org/10.1016/j.fuel.2017.03.006.
8. Kumar A, Kumar A, Biswas B, Kumar J, Yenumala SR, Bhaskar T. Hydrodeoxygenation of m-Cresol over Ru based catalysts: Influence of catalyst support on m-Cresol conversion and methylcyclohexane selectivity. Renew Energ. 2020;151:687-97. https://doi.org/10.1016/j.renene.2019.11.076.
9. Isa KM, Abdullah TAT, Ali UFM. Hydrogen donor solvents in liquefaction of biomass: A review. Renew Sustain Energ Rev. 2018;81:1259-68. https://doi.org/10.1016/j.rser.2017.04.006.
10. Guan W, Tsang CW, Lin CSK, Len C, Hu H, Liang C. A review on high catalytic efficiency of solid acid catalysts for lignin valorization. Bioresour Technol. 2020;298:122432. https://doi.org/10.1016/j.biortech.2019.122432.

11. Li B, Liu Y, Li R, Yang T, Kai X. Aluminum-water reactions assisted in situ hydrodeoxygenation of enzymolysis lignin from bioconversion of rice straw over NiMo catalyst. Ind Crop Prod. 2020;154:112727. https://doi.org/10.1016/j.indcrop.2020.112727.
12. Priharto N, Ronsse F, Prins W, Hita I, Deuss PJ, Heeres HJ. Hydrotreatment of pyrolysis liquids derived from second-generation bioethanol production residues over NiMo and CoMo catalysts. Biomass Bioenerg. 2019;126:84-93. https://doi.org/10.1016/j.biombioe.2019.05.005.
13. Kordouli E, Pawelec B, Kordulis C, Lycourghiotis A, Fierro JLG. Hydrodeoxygenation of phenol on bifunctional Ni-based catalysts: Effects of Mo promotion and support. Appl Catal B-Environ. 2018;238:147-60. https://doi.org/10.1016/j.apcatb.2018.07.012.
14. Wang C, Li Z, Wu K, Liu J, Yang X, Kong X et al. Synthesis of Ni–Mo–N catalysts for removing oxygen from acetophenone. Biomass Bioenerg. 2020;133:105448. https://doi.org/10.1016/j.biombioe.2019.105448.
15. Sangnikul P, Phanpa C, Xiao R, Zhang H, Reubroycharoen P, Kuchonthara P et al. Role of copper- or cerium-promoters on NiMo/γ-Al_2O_3 catalysts in hydrodeoxygenation of guaiacol and bio-oil. Appl Catal A-Gen. 2019;574:151-60. httpss://doi.org/10.1016/j.apcata.2019.02.004.
16. Appaturi JN, Adam F, Khanam Z. A comparative study of the regioselective ring opening of styrene oxide with aniline over several types of mesoporous silica materials. Micropor Mesopor Mat. 2012;156:16-21.

https://doi.org/10.1016/j.micromeso.2012.01.023.

17. Ambursa MM, Sudarsanam P, Voon LH, Hamid SBA, Bhargava SK. Bimetallic Cu-Ni catalysts supported on MCM-41 and Ti-MCM-41 porous materials for hydrodeoxygenation of lignin model compound into transportation fuels. Fuel Process Technol. 2017;162:87-97. https://doi.org/10.1016/j.fuproc.2017.03.008.
18. Totong S, Daorattanachai P, Laosiripojana N, Idem R. Catalytic depolymerization of alkaline lignin to value-added phenolic-based compounds over Ni/CeO_2-ZrO_2 catalyst synthesized with a one-step chemical reduction of Ni species using $NaBH_4$ as the reducing agent. Fuel Process Technol. 2020;198. https://doi.org/10.1016/j.fuproc.2019.106248.
19. Lin K, Pescarmona PP, Vandepitte H, Liang D, Van Tendeloo G, Jacobs PA. Synthesis and catalytic activity of Ti-MCM-41 nanoparticles with highly active titanium sites. J Catal. 2008;254:64-70. https://doi.org/10.1016/j.jcat.2007.11.017.
20. Wu JF, Ramanathan A, Biancardi A, Jystad AM, Caricato M, Hu Y et al. Correlation of Active Site Precursors and Olefin Metathesis Activity in W-Incorporated Silicates. ACS Catal. 2018;8:10437-45. https://doi.org/10.1021/acscatal.8b03263.
21. Yang XL, Gao R, Dai WL, Fan K. Influence of tungsten precursors on the structure and catalytic properties of WO_3/SBA-15 in the selective oxidation of cyclopentene to glutaraldehyde. J Phys Chem C. 2008;112:3819-26. https://doi.org/10.1021/jp710409g.
22. Popova M, Szegedi Á, Németh P, Kostova N, Tsoncheva T. Titanium modified

547 MCM-41 as a catalyst for toluene oxidation. Catal Commun. 2008;10:304-8.
548 https://doi.org/10.1016/j.catcom.2008.09.008.
549 23. Anunziata OA, Beltramone AR, Cussa J. Synthesis at atmospheric pressure and
550 characterization of highly ordered Al, V, and Ti-MCM-41 mesostructured catalysts.
551 Catal Today. 2008;133-135:891-6. https://doi.org/10.1016/j.cattod.2007.12.086.
552 24. Wang S, Ma C, Shi Y, Ma X. Ti incorporation in MCM-41 mesoporous molecular
553 sieves using hydrothermal synthesis. Front Chem Sci Eng. 2014;8:95-103.
554 https://doi.org/10.1007/s11705-014-1405-2.
555 25. Rao KS, El-Hami K, Kodaki T, Matsushige K, Makino K. A novel method for
556 synthesis of silica nanoparticles. J Colloid Interf Sci. 2005;289:125-31.
557 https://doi.org/10.1016/j.jcis.2005.02.019.
558 26. Gianotti E, Dellarocca V, Marchese L, Martra G, Coluccia S, Maschmeyer T. NH3
559 adsorption on MCM-41 and Ti-grafted MCM-41. FTIR, DR UV-Vis-NIR and
560 photoluminescence studies. Phys Chem Chem Phys. 2002;4:6109-15.
561 https://doi.org/10.1039/b207231a.
562 27. Méndez FJ, Bravo-Ascención G, González-Mota M, Puente-Lee I, Bokhimi X,
563 Klimova TE. NiMo catalysts supported on Al, Nb, Ti or Zr-containing MCM-41
564 for dibenzothiophene hydrodesulfurization. Catal Today. 2020;349:217-27.
565 https://doi.org/10.1016/j.cattod.2018.03.039.
566 28. Chen X, Liu J, Yan H, Zhou X, Yao S, Wang Y et al. Insight into the Effect of Lewis
567 Acid of W/Al-MCM-41 Catalyst on Metathesis of 1-Butene and Ethylene. Appl
568 Catal A-Gen. 2020;604:117772. https://doi.org/10.1016/j.apcata.2020.117772.

29. Carniti P, Gervasini A, Marzo M. Silica–niobia oxides as viable acid catalysts in water: Effective vs. intrinsic acidity. Catal Today. 2010;152:42-7. https://doi.org/10.1016/j.cattod.2009.07.111.

30. Zhang S, Su L, Liu L, Fang G. Degradation on hydrogenolysis of soda lignin using $CuO/SO_4^{2-}/ZrO_2$ as catalyst. Ind Crop Prod. 2015;77:451-7. https://doi.org/10.1016/j.indcrop.2015.07.039.

31. Lu M, Jiang Y, Sun Y, Zhang P, Zhu J, Li M et al. Hydrodeoxygenation of Guaiacol Catalyzed by ZrO_2–CeO_2-Supported Nickel Catalysts with High Loading. Energ Fuel. 2020;34:4685-92. https://doi.org/10.1021/acs.energyfuels.0c00445.

32. Mokaya R, Jones W. Physicochemical Characterisation and Catalytic Activity of Primary Amine Templated Aluminosilicate Mesoporous Catalysts. J Catal. 1997;172:211-21. https://doi.org/10.1006/jcat.1997.1851.

33. Mendez FJ, Bravo-Ascencion G, Gonzalez-Mota M, Puente-Lee I, Bokhimi X, Klimova TE. NiMo catalysts supported on Al, Nb, Ti or Zr-containing MCM-41 for dibenzothiophene hydrodesulfurization. Catal Today. 2020;349:217-27. httpss://doi.org/10.1016/j.cattod.2018.03.039.

34. Ambursa MM, Sudarsanam P, Voon LH, Abd Hamid SB, Bhargava SK. Bimetallic Cu-Ni catalysts supported on MCM-41 and Ti-MCM-41 porous materials for hydrodeoxygenation of lignin model compound into transportation fuels. Fuel Process Technol. 2017;162:87-97. https://doi.org/10.1016/j.fuproc.2017.03.008.

35. Kordouli E, Pawelec B, Kordulis C, Lycourghiotis A, Fierro JLG. Hydrodeoxygenation of phenol on bifunctional Ni-based catalysts: Effects of Mo

promotion and support. Appl Catal B-Environ. 2018;238:147-60. https://doi.org/10.1016/j.apcatb.2018.07.012.

36. Spanos N, Vordonis L, Kordulis C, Lycourghiotis A. Molybdenum-oxo species deposited on alumina by adsorption: I. Mechanism of the Adsorption. Journal of Catalysis. 1990;124:301-14. https://doi.org/10.1016/0021-9517(90)90179-N.
37. Dzwigaj S, Louis C, Breysse M, Cattenot M, Bellière V, Geantet C et al. New generation of titanium dioxide support for hydrodesulfurization. Appl Catal B-Environ. 2003;41:181-91. https://doi.org/10.1016/S0926-3373(02)00210-2.
38. Gao J, Zheng Y, Jehng JM, Tang Y, Wachs IE, Podkolzin SG. Identification of molybdenum oxide nanostructures on zeolites for natural gas conversion. Science. 2015;348:686. https://doi.org/10.1126/science.aaa7048.
39. Rynkowski JM, Paryjczak T, Lenik M. On the nature of oxidic nickel phases in NiO/γ-Al_2O_3 catalysts. Appl Catal A-Gen. 1993;106:73-82. https://doi.org/10.1016/0926-860X(93)80156-K.
40. Bakhtyari A, Sakhayi A, Rahimpour MR, Raeissi S. Upgrading of cyclohexanone to hydrocarbons by hydrodeoxygenation over nickel–molybdenum catalysts. Int J Hydrogen Energ. 2020;45:11062-76. https://doi.org/10.1016/j.ijhydene.2020.02.036.
41. Zhang X, Wang T, Ma L, Zhang Q, Yu Y, Liu Q. Characterization and catalytic properties of Ni and NiCu catalysts supported on ZrO_2–SiO_2 for guaiacol hydrodeoxygenation. Catal Commun. 2013;33:15-9. https://doi.org/10.1016/j.catcom.2012.12.011.

42. Fogassy G, Thegarid N, Schuurman Y, Mirodatos C. From biomass to bio-gasoline by FCC co-processing: effect of feed composition and catalyst structure on product quality. Energ Environ Sci. 2011;4:5068-76. https://doi.org/10.1039/c1ee02012a.
43. Zhang H, Cheng Y-T, Vispute TP, Xiao R, Huber GW. Catalytic conversion of biomass-derived feedstocks into olefins and aromatics with ZSM-5: the hydrogen to carbon effective ratio. Energ Environ Sci. 2011;4:2297-307. https://doi.org/10.1039/c1ee01230d.
44. Chen N, Gong S, Qian EW. Effect of reduction temperature of $NiMoO_3$-x/SAPO-11 on its catalytic activity in hydrodeoxygenation of methyl laurate. Appl Catal B-Environ. 2015;174-175:253-63. https://doi.org/10.1016/j.apcatb.2015.03.011.
45. Olcese RN, Bettahar M, Petitjean D, Malaman B, Giovanella F, Dufour A. Gas-phase hydrodeoxygenation of guaiacol over Fe/SiO_2 catalyst. Appl Catal B-Environ. 2012;115-116:63-73. https://doi.org/10.1016/j.apcatb.2011.12.005.
46. Lu X, Dai P, Zhu X, Guo H, Que H, Wang D et al. Thermal behavior and kinetics of enzymatic hydrolysis lignin modified products. Thermochim Acta. 2020;688. https://doi.org/10.1016/j.tca.2020.178593.
47. Alves A, Schwanninger M, Pereira H, Rodrigues J. Analytical pyrolysis as a direct method to determine the lignin content in wood - Part 1: Comparison of pyrolysis lignin with Klason lignin. J Anal Appl Pyrol. 2006;76:209-13. https://doi.org/10.1016/j.jaap.2005.11.004.
48. Mendez FJ, Bastardo-Gonzalez E, Betancourt P, Paiva L, Brito JL. NiMo/MCM-41 Catalysts for the Hydrotreatment of Polychlorinated Biphenyls. Catalysis

Letters. 2013;143:93-100. https://doi.org/10.1007/s10562-012-0933-y.

49. Lup ANK, Abnisa F, Daud WMAW, Aroua MK. Synergistic interaction of metal-acid sites for phenol hydrodeoxygenation over bifunctional Ag/TiO_2 nanocatalyst. Chinese J Chem Eng. 2019;27:349-61. https://doi.org/10.1016/j.cjche.2018.08.028.

Table object

Table 1 Physical properties and acid strength of synthesized catalysts.

Catalyst	S_{BET}	V_{pore}	S_{pore}	Ti[a]	W[a]	Acidity (mmol NH_3 g^{-1} catalyst)			
	(m^2 g^{-1})	(cm^3 g^{-1})	(Å)	(wt%)	(wt%)	Total[c]	Weak[b]	Medium[b]	Strong[b]
SiO_2-NC	28.1	0.07	42.1	-	-	-	-	-	-
SiO_2-C	654.2	0.52	32.0	-	-	0.170	0.151 (88.8 %)	0.012 (7.1 %)	0.007 (4.1 %)
Ti-SiO_2	375.7	0.32	31.7	2.28	-	0.339	0.308 (90.9 %)	0.024 (7.1 %)	0.007 (2.0 %)
W-SiO_2	413.8	0.32	30.5	-	6.82	0.485	0.392 (80.8 %)	0.081 (16.7 %)	0.012 (2.5 %)

S_{BET} - the surface area measured by BET method.

V_{pore} - the volume of pore.

S_{pore} - the size of pore.

[a] Determined by ICP-OES.

[b] Weak, medium, strong acidity (< 200 ºC, ~ 300 ºC, > 400 ºC).

[c] Determined by NH_3-TPD.

Table 2. Physical properties of spent catalyst and reactivated one.

Catalyst	S_{BET} (m^2 g^{-1})	V_{pore} (cm^3 g^{-1})	S_{pore} (Å)	W[a] (wt%)	Ni[a] (wt%)	Mo[a] (wt%)	Lignin conversion (wt%)	Bio-oil (wt%)	Char (wt%)
Fresh	325.8	0.27	30.1	6.82	28.5	40.1	66.3	57.2	9.1
Reuse-1	273.4	0.18	35.2	6.64	27.3	39.4	62.1	52.9	9.2
Reuse-2	241.2	0.16	37.1	6.55	27.1	39.1	60.3	51.6	8.7
Reuse-3	218.3	0.15	35.6	6.52	26.4	39.0	58.3	49.8	8.5
Reuse-4	211.2	0.17	34.9	6.44	26.1	38.5	54.9	46.7	8.2
Reuse-5	211.4	0.12	37.2	6.38	26.1	37.8	52.5	44.4	8.1
Reactivation	321.2	0.26	30.2	6.33	25.3	37.4	63.2	54.2	9.0

[a] Determined by ICP-OES.

Table 3. Proximate, ultimate, and component analyses of raw and extracted lignin.

Sample	Proximate analysis[a] (wt%)				Ultimate analysis[c] (wt%)				Lignin
	Moisture	Ash	Volatile matter	Fixed carbon[b]	C	H	O[b]	N	content[d, e] (wt%)
Raw lignin	5.6	2.7	71.5	20.2	46.7	7.1	45.3	0.9	80.2
Extracted lignin	4.9	2.5	74.3	18.3	47.4	7.3	44.7	0.6	98.8

[a] Measured by ASTM Standard Test Method E. 1690-01.

[b] Calculated by difference.

[c] Ash and moisture free.

[d] On dry basis.

[e] Determined by Klason method [47].

Figures

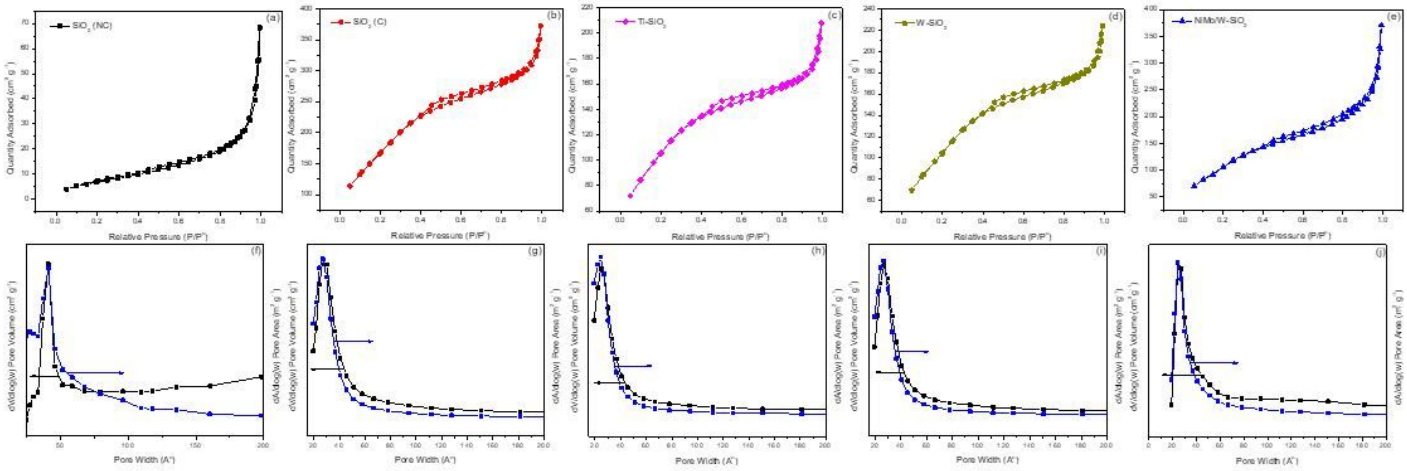

Figure 1

N2 adsorption-desorption isotherms of SiO2-NC (a, uncalcined), SiO2-C (b, calcined), Ti-SiO2 (c), W-SiO2 (d), and NiMo/W-SiO2 (e). Respective pore size distributions of different samples (f: SiO2-NC, g: SiO2-C, h: Ti-SiO2, i: W-SiO2, and j: NiMo/W-SiO2).

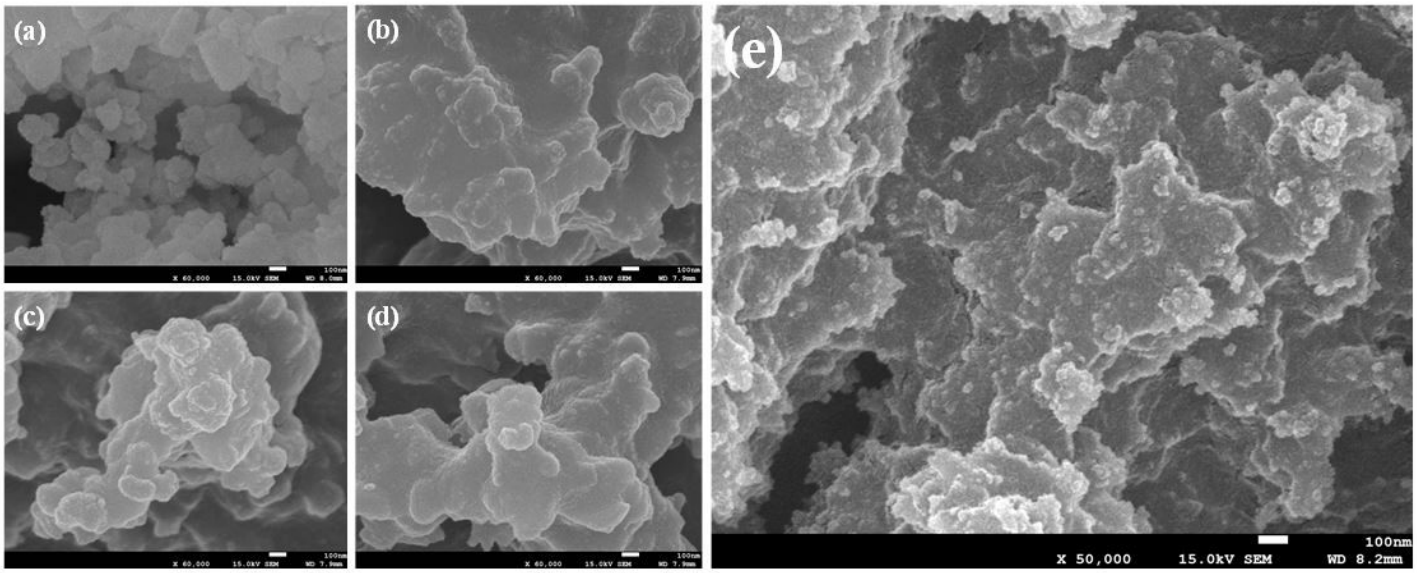

Figure 2

SEM images of SiO2-NC (a), SiO2-C (b), Ti-SiO2 (c), W-SiO2 (d), and NiMo/W-SiO2 (e).

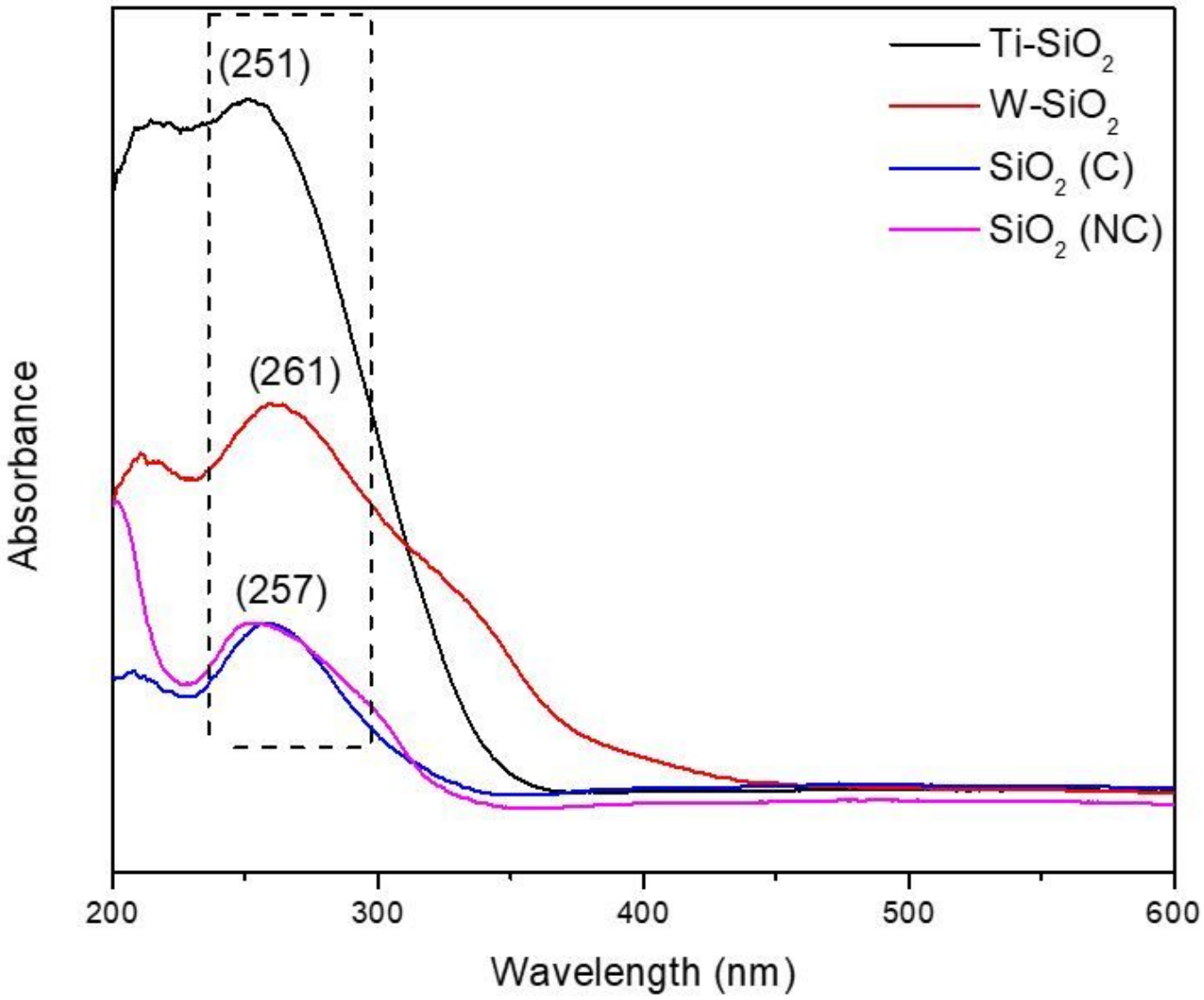

Figure 3

UV-visible diffuse reflectance spectra (DRS) of supports.

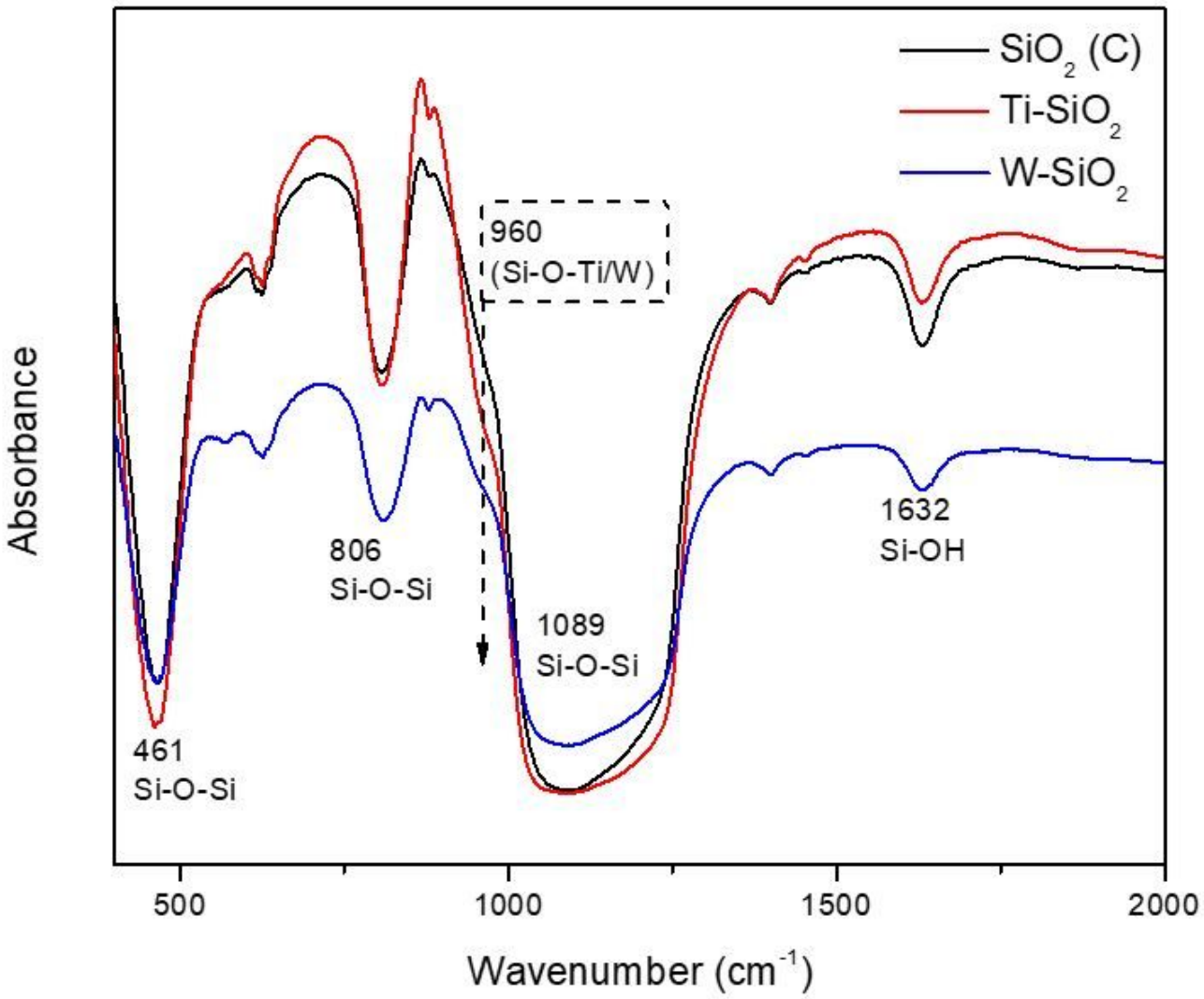

Figure 4

FTIR spectra of synthesized supports.

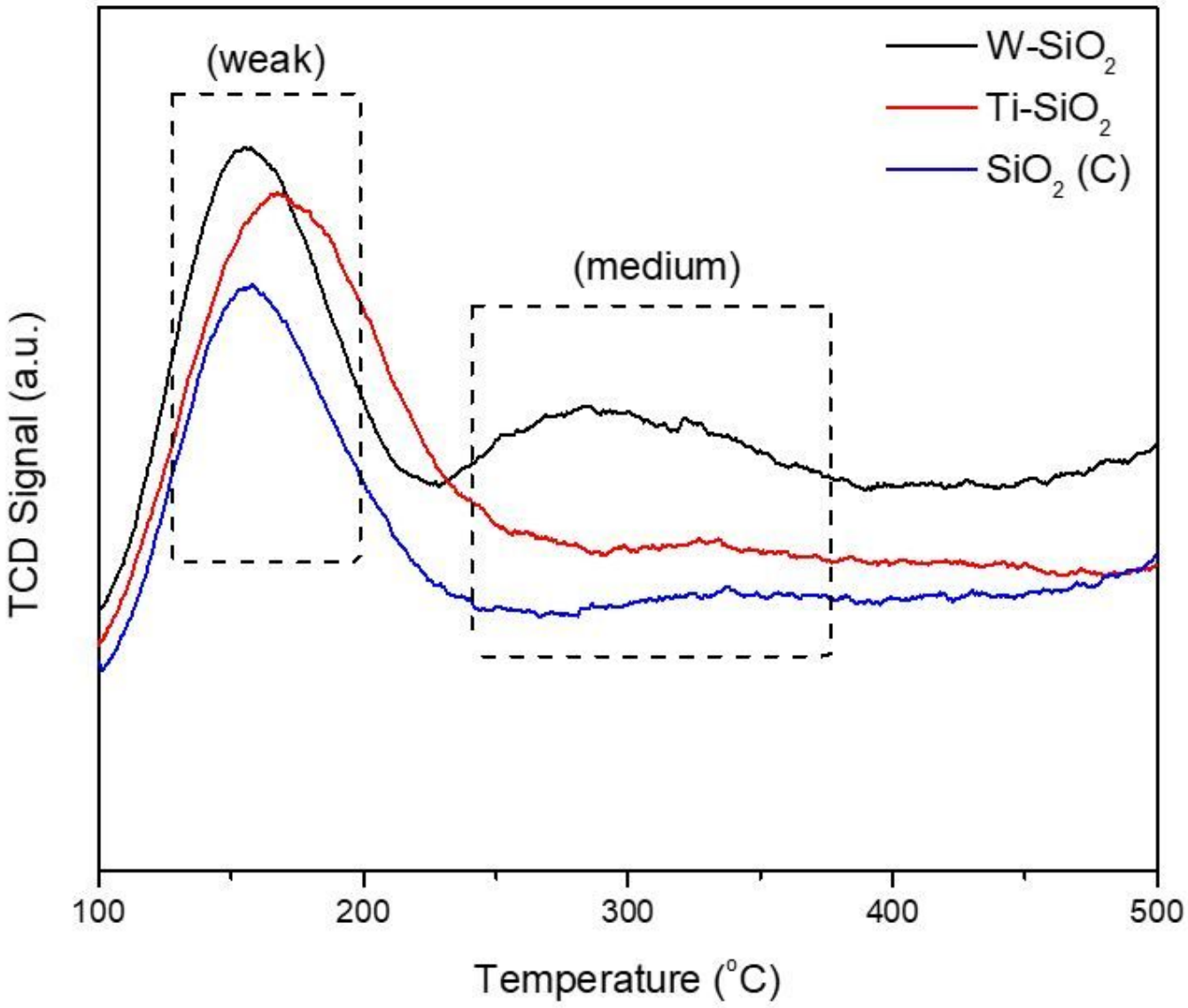

Figure 5

NH3-TPD of SiO2-C (blue line), Ti-SiO2 (red line), and W-SiO2 (black line).

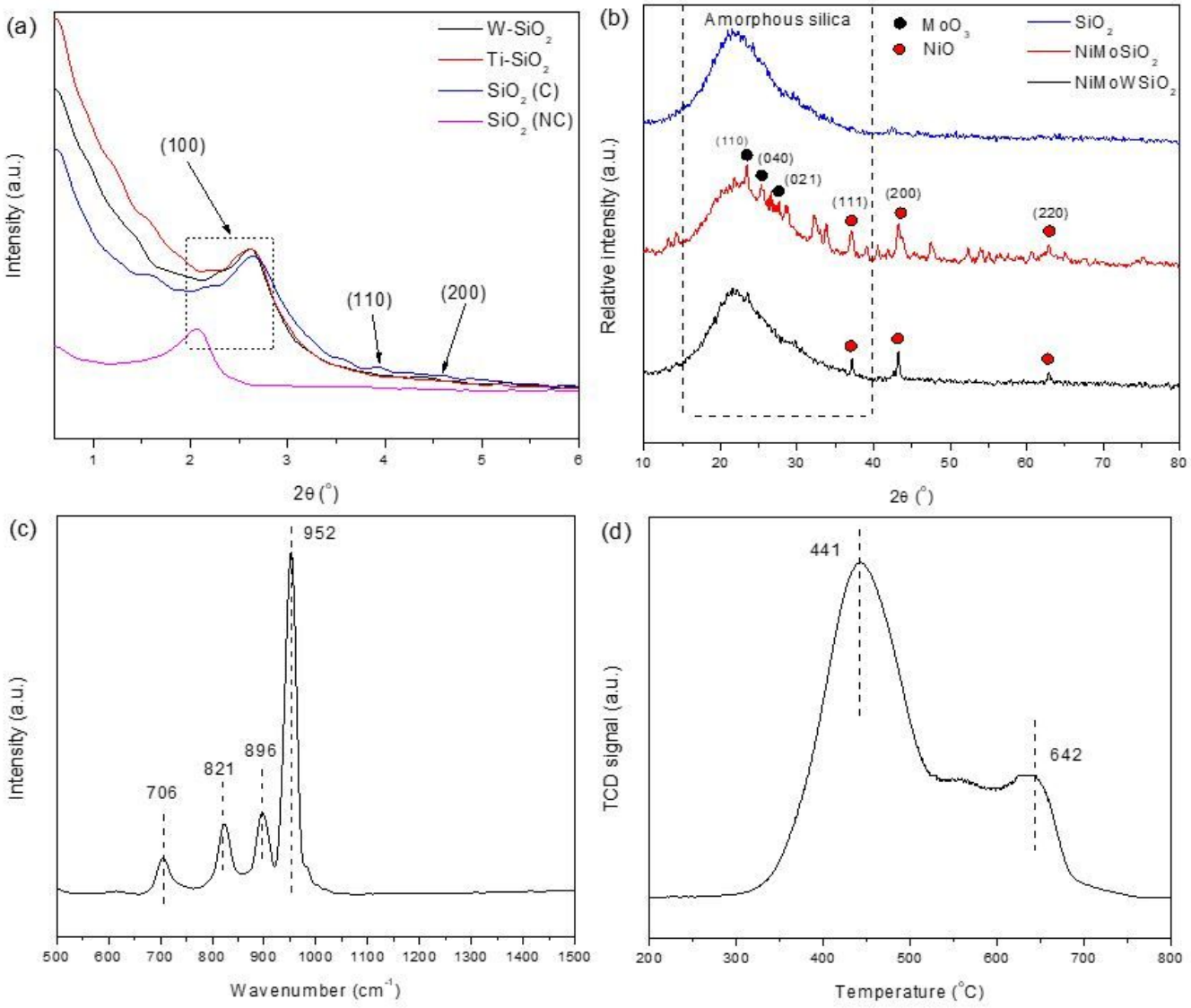

Figure 6

(a) SA-XRD patterns of support and catalysts, (b) WA-XRD patterns of support and NiMo supported catalysts, (c) Raman spectrum of NiMo/W-SiO2, and (d) H2-TPR profile of NiMo/W-SiO2.

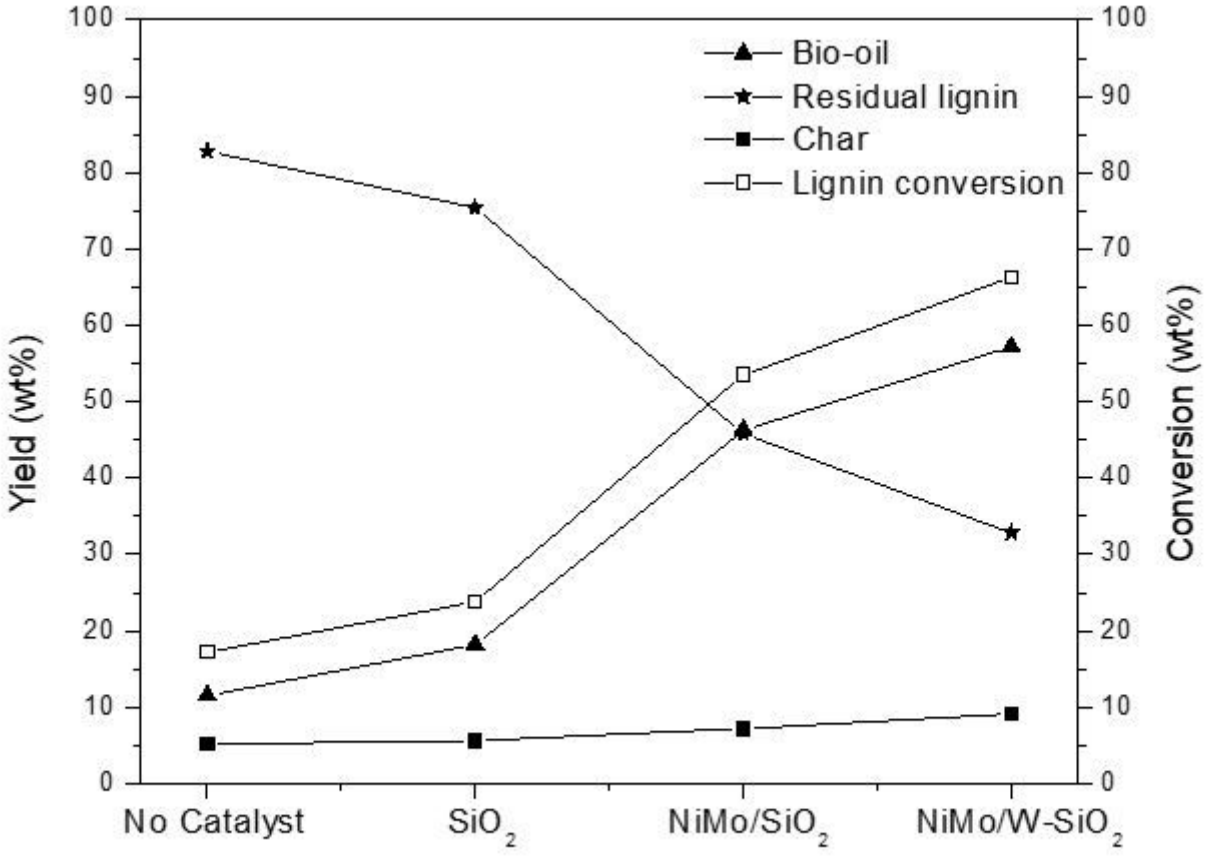

Figure 7

Catalytic evaluation of lignin depolymerization over different synthesized catalysts.

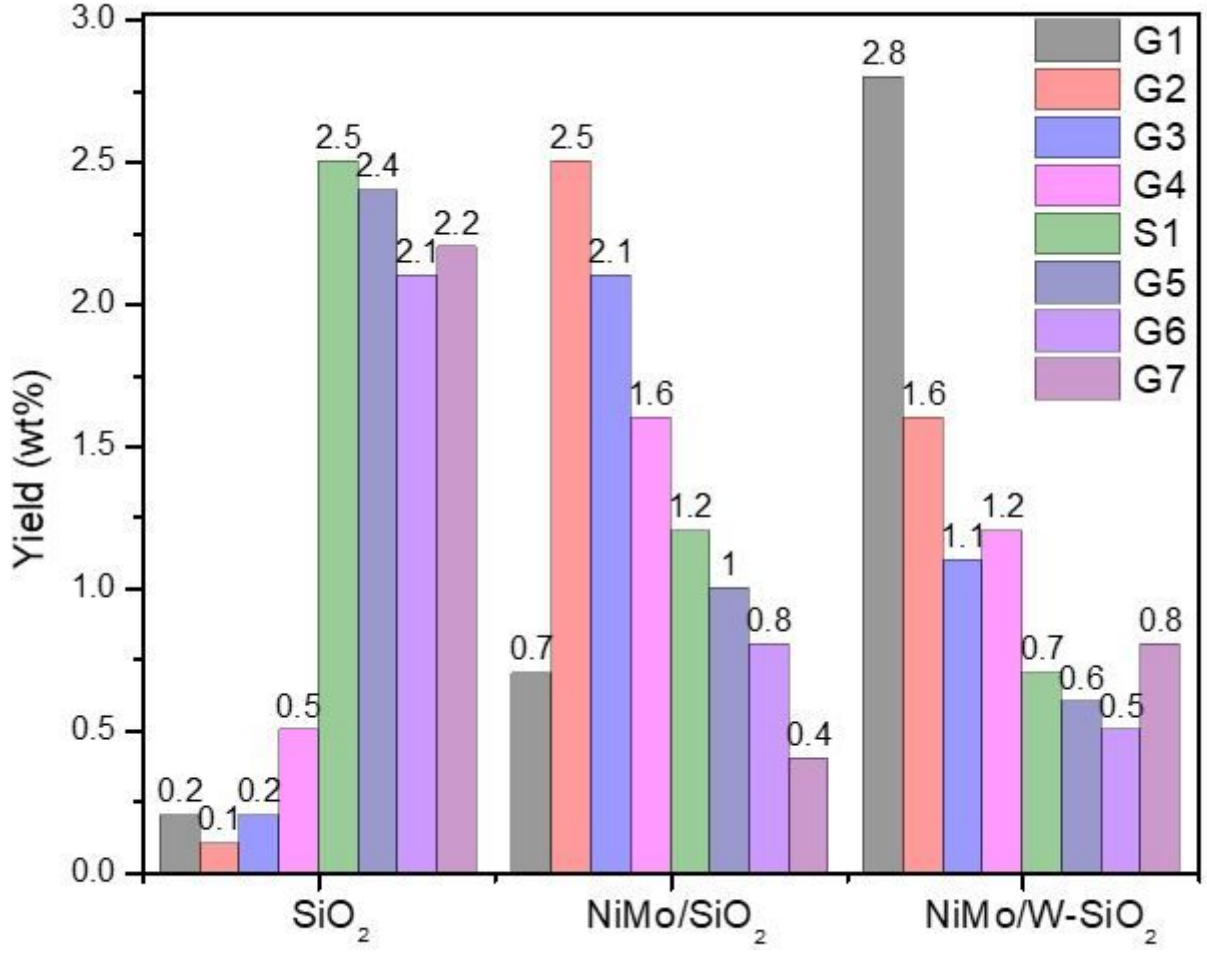

Figure 8

The main monomers (wt%) produced from lignin depolymerization over NiMo/W-SiO2 (G1: guaiacol, G2: 2-methoxy-4-methylphenol, G3: 4-ethylguaiacol, G4: 2-methoxy-4-(1-propyl)phenol, S1: 2,6-dimethoxyphenol, G5: vanillin, G6: 4-hydroxy-3-methoxyacetophenone, G7: 4-hydroxy-3-methoxypropiophenone).

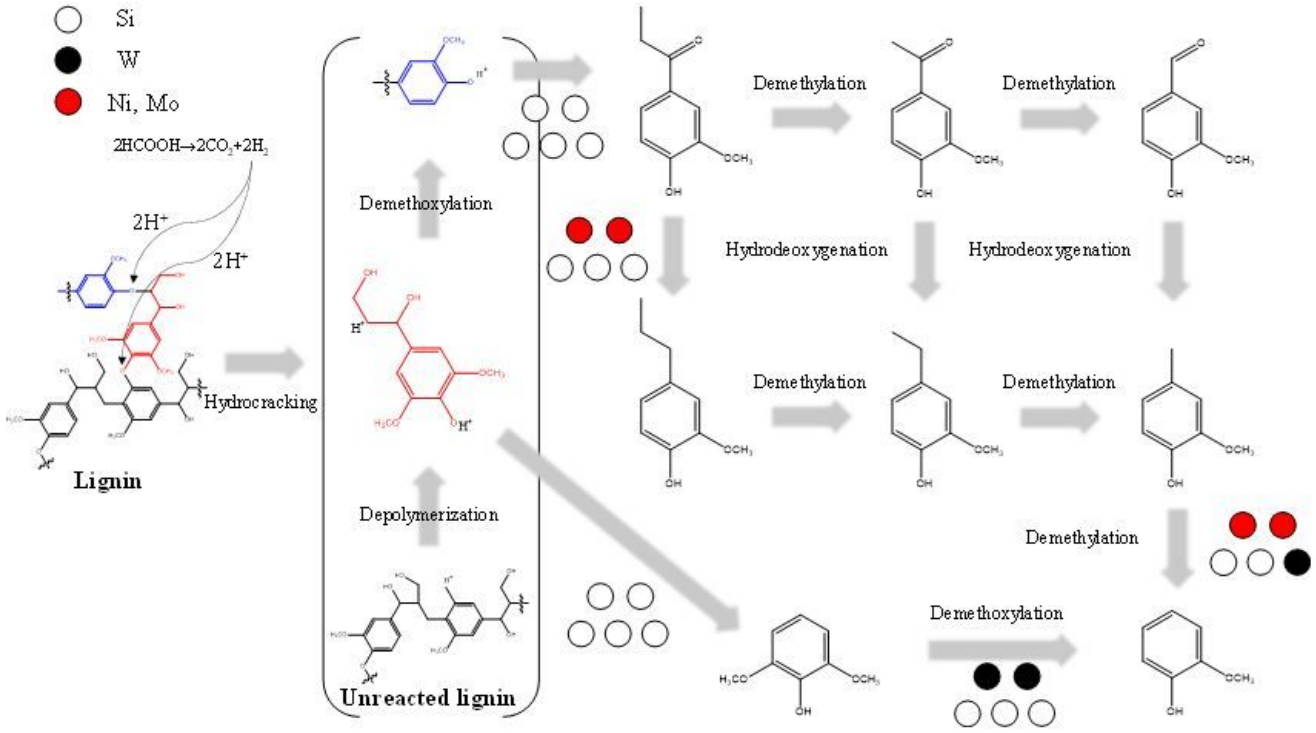

Figure 9

Possible reaction mechanism of lignin depolymerization over supported metal catalysts with assistance of formic acid used as an internal hydrogen donor.

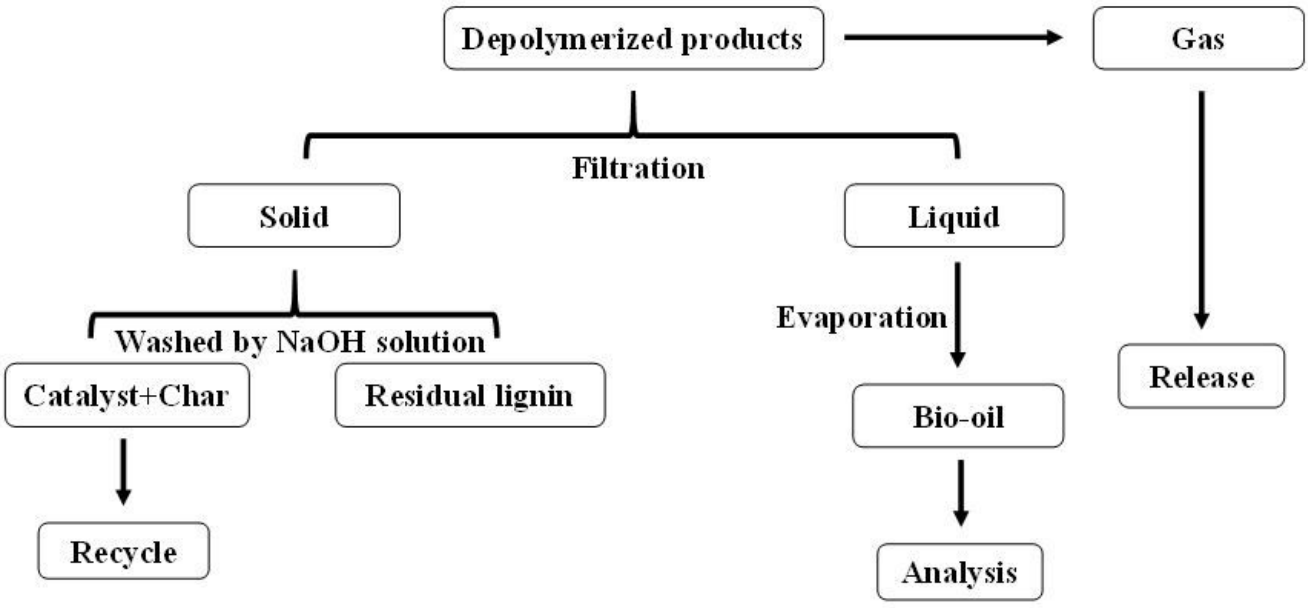

Figure 10

Separation steps of depolymerized phases.